Reconstructing a solid-solid phase transformation pathway in CdSe nanosheets with associated soft ligands

Zhongwu Wang[a,1], Xiao-Dong Wen[b], Roald Hoffmann[b,1], Jae Sung Son[c], Ruipeng Li[a], Chia-Chen Fang[d], Detlef-M. Smilgies[a], and Taeghwan Hyeon[c]

[a]Cornell High Energy Synchrotron Source (CHESS), Wilson Laboratory, Cornell University, Ithaca, NY 14853; [b]Department of Chemistry and Chemical Biology, Cornell University, Ithaca, NY 14853; [c]National Creative Research Initiative Center for Oxide Nanocrystalline Materials and School of Chemical and Biological Engineering, Seoul National University, Seoul 151-744, Korea; and [d]Department of Materials Science and Engineering, Cornell University, Ithaca, NY 14853

Integrated single-crystal-like small and wide-angle X-ray diffraction images of a CdSe nanosheet under pressure provide direct experimental evidence for the detailed pathway of transformation of the CdSe from a wurtzite to a rock-salt structure. Two consecutive planar atomic slips [(001) $\langle 110 \rangle$ in parallel and (102) $\langle \bar{1}01 \rangle$ with a distortion angle of ~40°] convert the wurtzite-based nanosheet into a saw-like rock-salt nanolayer. The transformation pressure is three times that in the bulk CdSe crystal. Theoretical calculations are in accord with the mechanism and the change in transformation pressure, and point to the critical role of the coordinated amines. Soft ligands not only increase the stability of the wurtzite structure, but also improve its elastic strength and fracture toughness. A ligand extension of 2.3 nm appears to be the critical dimension for a turning point in stress distribution, leading to the formation of wurtzite (001)/zinc-blende (111) stacking faults before rock-salt nucleation.

phase transition | semiconductor | dimensionality

Rational synthesis of materials with defined structure and properties requires a reasonably complete understanding of the associated kinetic transformations and microscopic mechanisms (1). We need to know these in order to understand how associated soft-bonded organics may tune structural stability, elastic strength, and fracture toughness (1–3). The study of solid-solid phase transformations of materials, and their structural stabilization upon incorporation of soft materials at different scales, can be very helpful in this regard. For instance, application of pressure and temperature converts graphite to a hard diamond phase that persists at ambient conditions, allowing for a wide range of known applications (4). Upon addition of soft materials such as silicon and metals (5, 6), the sintered diamond-dominant nanocomposites show improved yield strength and fracture toughness (by several orders of magnitude) without significant diminution of hardness.

Many fascinating natural substances, such as human bone and other biological materials, also contain exceptionally strong building blocks (2, 3) essential to their function. The subtle interplay between soft organics and embedded brittle materials is responsible not only for enhancement of the structural stability of embedded brittle materials, but also for improvement of the yield strength and fracture toughness of assembled hierarchical organizations (2, 3).

Microscopic mechanisms of transformation are difficult to determine. In bulk solids, as metastable higher energy and higher density phases nucleate in multiple domains, structural features (such as defects, microstructure, and impurities) may modify significantly the kinetics and mechanism of a phase transformation. In principle, calculations could provide the energy difference between structural polymorphs at a given pressure or temperature. But putting aside problems in computing activation barriers,

there is often a large discrepancy between theory and experiment. For instance, the nucleation pressure of the bulk zinc-blende to rock-salt ZnS phase transformation (with variable microstructure and lattice strain) was observed over a wide pressure range, $8 \sim 16$ GPa (7–11). However, the calculated thermodynamic transformation pressure was $14.7 \sim 16.1$ GPa (12–14).

To avoid the effect of structural peculiarities on transformation mechanism, one should ideally carry out measurements on a perfect defect-free crystal. Small nanocrystals behave as defect-free small crystals in which a single domain dominates the nucleation of another structure phase. In a defect-free nanocrystal, if we exclude the contribution of the size-dependent surface energy, the experimental transformation pressure should be equivalent to the calculated transformation pressure (15). One supportive example is that an observed transformation pressure of 15.1 GPa in 15 nm zinc-blende ZnS agrees well with the calculated transformation pressure (15); 15 nm in zinc-blende ZnS proves to be a critical size for nanoparticles to behave like a defect-free bulk crystal (16, 17). [We used theories developed in the literature (16, 17) to define the two critical sizes of 15 nm and 4 nm for zinc-blende ZnS. These appear to be the turning point for the particle to be strain-insensitive and defect-free, respectively (15).]

In this context, the Alivisatos group has performed a rich spectrum of measurements on spherical CdSe nanoparticles using synchrotron X-ray diffraction and optical spectroscopy at well-controlled pressure and temperature (18–21). The observed transformation pressure as a function of particle size, and the pressure dependence of the relaxation time provide ways to determine the activation volume and barrier height (for the wurtzite → rock-salt phase transformation) (9). Several models for the transformation were then derived, leading to a reasonable description of the microscopic mechanisms (18, 21). However, one is still not sure experimentally of the true pathway, because a comparison of a measured X-ray diffraction (XRD) pattern with several simulated patterns (necessary because of different microstructural assumptions in simulations) is required (21). In parallel investigations, theoretical simulations have suggested several subtle steps that were not included in the proposed transformation pathways (22–24). One might not know whether to trust theory or experiment here; an experimental key is lacking to open this black box and single out the true transformation pathway.

In this study, we show that a technique integrating in situ small-angle X-ray diffraction (SAXRD) and wide-angle X-ray diffraction (WAXRD) can identify the preferred sample orientation and elucidate quite precise details of the phase transformation mechanism of CdSe nanosheets. [In Fig. 1, we use one SAXRD image taken at high pressure in which a full texture is shown for better understanding. This is because a large beam stop was used in the X-ray diffraction image collection at 0 GPa for detector protection. Thus half the diffraction ring (*Inset* SAXRD) was blocked.]

Results and Discussion

1. Experiments and Transformation Pathway. Highly uniform 1.4-nm-thick CdSe nanosheets have been shown to have a defect-free wurtzite structure with a (001) growth direction (25, 26). [In hexagonal crystal systems, there are two conventions for labeling crystal planes, a three-index and a four-index label. In this paper, we consistently use the three-index notation. CdSe(001) = 0001; CdSe(110) = (11$\bar{2}$0).] Two (110) facets dominate the top and bottom surfaces; (001) facets terminate the two side surfaces. The CdSe nanosheets are not pristine; bonded to the (110) surfaces are organic ligands of octylamine or oleylamine or some mixture of these. There are van der Waals forces between CdSe nanosheets, and these lead to lamellar mesostructure (26). [The CdSe nanosheets bonded at their surface with several types of ligands that have different chain lengths were synthesized by a low-temperature solution chemical synthesis (25, 26). The length scale of each sample was characterized by SAXRD.]

The highly oriented samples display a single-crystal-like XRD image, indicating that the lamellar superstructure CdSe nanosheets are loaded with expected orientations into a diamond anvil cell (DAC). The in situ synchrotron XRD diffraction images collected under pressure reveal a series of pressure- or transformation-tuned texture changes. These allow precise tracking of the position and magnitude of atomic distortion and translation during the wurtzite ↔ rock-salt structural transformation.

Fig. 1 shows the SAXRD and WAXRD images that correspond to the shape and lattice of lamellar CdSe nanosheets in our experiment. Two single-crystal-like broad diffraction spots in the SAXRD image reveal that the basal lamellar layer is parallel to the force-loading axis of DAC (incident X-ray direction). Correlating the lattice structure of CdSe nanosheets, the WAXRD image indicates that either the (100) or (001) plane is parallel to the diamond anvil surface. The strong spotty diffraction characteristics develop at (002) rather than at (100); this indicates that the (100) plane prefers to be oriented parallel to the
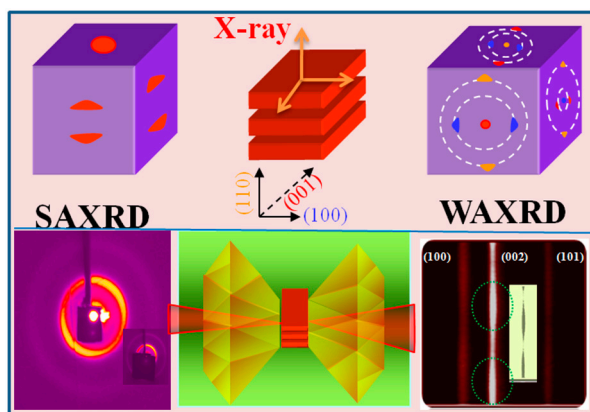
diamond anvil. Following such alignment, a lattice orientation was tuned with the (100) plane perpendicular, and both (110) and (001) planes parallel to the incident X-ray beam.

The SAXRD and WAXRD measurements on the CdSe samples (terminated by a mixture of octylamine and oleylamine, as analyzed in *SI Text* and Fig. S1) were then carried out over a pressure range of 0–12.7 GPa. The WAXRD images (Fig. 2A) indicate that wurtzite CdSe transforms to a rock-salt structure at ~10.7 GPa, a pressure significantly greater than the transformation pressure of 2.5 GPa observed in bulk CdSe (18). It is worth noting that the wurtzite (002)/zinc-blende (111) stacking fault was not detected before the nucleation of the rock-salt phase.

Upon decompression, a mixture of wurtzite and zinc blende is observed at 3.1 GPa. On further release of pressure, a single wurtzite phase is fully recovered (Fig. 2B). However, in bulk and other nanocrystal CdSe samples, the CdSe recovered from high pressure always has the zinc-blende structure (3), no matter whether the starting CdSe sample crystallizes in a wurtzite or zinc-blende structure. The SEM characterization indicates that pressure and phase transformation do not result in a noticeable fracture of the nanosheet; the coexistence of zinc blende and wurtzite is observed at 3.1 GPa. Most likely one is seeing a series of wurtzite (002)/zinc-blende (111) stacking faults across the original (001) growth direction of the nanosheet.

An azimuthal plot of typical WAXRD images reveals that CdSe nanosheets produce two strong single-crystal-like diffraction spots located on the W (002) ring (Fig. 3A). In Fig. 3A, the notation is W = wurtzite, RS = rock salt, and Z = zinc blende. Upon phase transformation at 10.7 GPa, two similar diffraction spots are assigned to the nucleated rock-salt (111) ring and are developed from the two W (002) spots at a shift angle of ~40° (Fig. 3A). Relative to the RS (111) spots, the two RS (200) spots emerge at a rotation angle of 55° and 23°, respectively. Releasing the pressure to 3.1 GPa, the two diffraction spots on the overlapping ring of Z (111) and W (002) appear at the same positions as the starting W (002) spots (Fig. 2A). In Fig. 3B, the WAXRD patterns of CdSe nanosheets with an intersheet distance of 2.3 nm at 8.1 GPa indicate the coexistence of zinc-blende, wurtzite, and rock-salt CdSe structures.

Using the experimental information on the way pressure tunes the rotation and translation magnitude of single-crystal-like XRD spots, the transformation pathway from wurtzite to rock salt in the nanosheets may be unambiguously reconstructed, as shown in Fig. 4 *A* and *B*.

There are two sliding steps in the transformation: (i) W CdSe activates the basal system (001)⟨110⟩. Pressure forces the Cd and Se atoms to slide relative to each other (move out and in of the plane) in the (001) plane (Fig. 4A). The sequence is similar to the known deformation mechanism in hcp-type metals (27). In prin-

Fig. 1. (*Top*) Theoretical correlation of SAXRD and WAXRD to the shape and lattice orientation of lamellar structure CdSe illuminated by an incident X-ray beam along different directions. (*Bottom, Left* and *Right*) Experimental diffraction images indicating the preferred orientations of 1.4-nm-thick CdSe nanosheets. The inset in the lower right-hand corner image highlights at high contrast the spotty feature of the (002) peak.

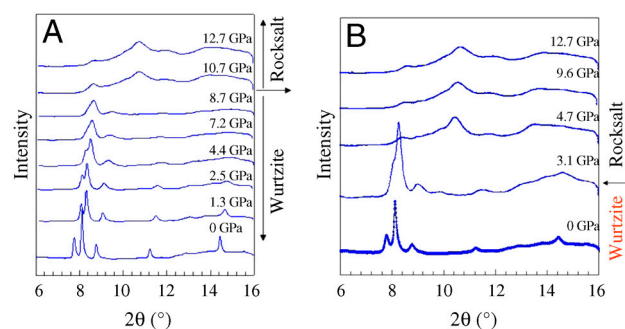**Fig. 2.** Representative high-pressure wide-angle X-ray diffraction patterns of lamellar CdSe nanosheets: (*A*) compression run, indicating that wurtzite transforms to rock salt at 10.7 GPa; (*B*) decompression run, indicating that the rock-salt structure of the CdSe nanosheet transforms to a mixture of zinc-blende and wurtzite structures at 3.1 GPa, and at 0 GPa is completely converted back to the wurtzite structure.
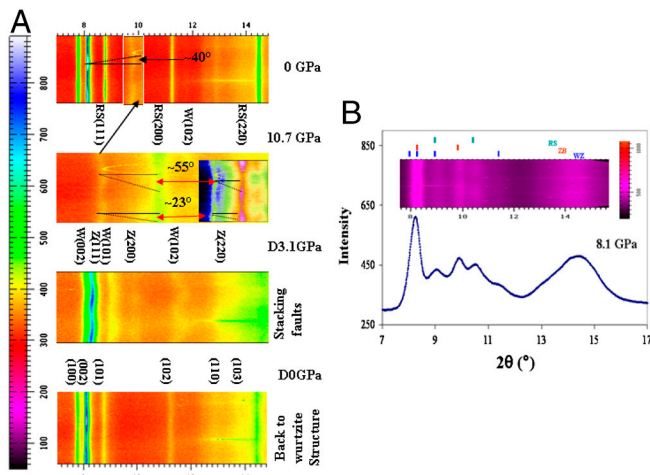
Fig. 3. Azimuthal plot of a typical in situ pressurized WAXRD image of the 1.4-nm-thick CdSe nanosheets, and the reconstructed transformation pathway from wurtzite to rocksalt. (*A*) Azimuthal plot of a typical WAXRD image of the CdSe nanosheet with an intersheet distance of 2.6 nm. (Note: inset at 10.7 GPa has increased contrast for improved definition of spotty texture; the horizontal strips are noise from diamond anvil surface.) (*B*) CdSe nanosheets with an intersheet distance of 2.3 nm at 8.1 GPa, showing the coexistence of rock salt, wurtzite, and zinc blende at the transition pressure. The (001) peak gives us the intersheet distance.

ciple, such a planar shift creates W (001)/Z (111) stacking faults; they are detected only in the "short-ligand"-bonded CdSe nanosheets, rather than the ones bonded to long ligands.

(*ii*) In the next step, the (102) plane atoms slide along the $\langle \bar{1}01 \rangle$ direction with an angle of 40°, producing the two observed shift angles of 55° and 23° (Fig. 3*A*). The first angle (55°) is consistent with the ideal intercepting angle of 54.7° between RS (200) and RS (111) (Fig. 4*B*). The other one (23°) is an approximate average of the two interception angles between groups of equivalent crystallographic planes [e.g., ($\bar{2}00$) and ($\bar{1}\,\bar{1}\,1$) vs. ($\bar{0}20$) and ($\bar{1}\,\bar{1}\,\bar{1}$)] in a rock-salt structure (see *SI Text* and Fig. S2).

The large lattice strain (revealed by the remnant of the highly textured W (102) ring in the rock-salt pattern in Fig. 2*A*) could explain the unsymmetrical occurrence of the second diffraction spot. The 3- and 4-fold axes in the rock-salt phase are rotated by 40° and 5° (or 15°) against the 6-fold axis of the starting wurtzite structure. The strain-free and highly strained environments lead to axial rotation by 5° and 15° (4-fold axis in RS against 6-fold axis in W), respectively (28, 29), explaining well the ambiguous observations contrasting bulk single crystal CdS (28) and CdSe (29). [In bulk single crystals, they observed a rotation angle of 5° and 15° from the 6-fold axis of wurtzite in CdS (28) and CdSe (29), respectively, to form the 4-fold axis of rock salt.]

2. Theoretical Simulations of the Phase Transition of CdSe Nanosheets.

Using density functional theory (DFT) periodic calculations as implemented in the Vienna ab initio simulation package (VASP) (see *SI Text* and Figs. S2–S8), organic ligands are embedded between slabs, bonding to cadmiums at the top and bottom surface
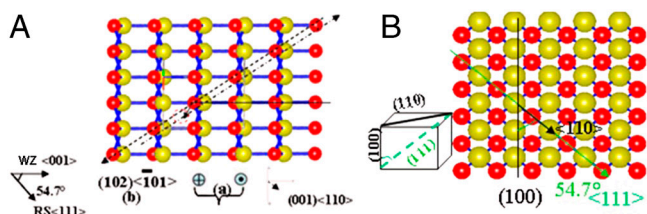

Fig. 4. (*A*) Two observed planar atomic slide types: type I—(001)⟨110⟩ and type II—(102)⟨101⟩. (*B*) The resulting rock-salt structure.

of the CdSe nanosheets. Methylamine is used by us as a model coordinating base in the calculations.

Beginning with a seven-layer CdSe slab model covered by methylamines at 0 GPa, we optimize the slab structure at 2.5 GPa, 5 GPa, 7 GPa, 8 GPa, and 15 GPa, respectively, of which at 2.5 GPa, 7 GPa, and 8 GPa are shown in Fig. 5. The CdSe layers and coordinated methylamine layers are apparent. Following the CdSe geometries, one can see that the wurtzite phase undergoes a transformation to a rock-salt phase at 8 GPa; the phase transformation is barrier-free. Because of the lack of an energy barrier to the reverse structural transformation route (rock salt → wurtzite), the pressure-tuned roc-ksalt CdSe phase cannot be retained at ambient conditions after compression. This is in agreement with our experimental observations.

It is remarkable that the transition (wurtzite → rock salt) in 2D nanosheets occurs at ~3 times higher pressure than that necessary for transforming the bulk structures. The calculated transition pressure of 2.5 GPa for bulk structure agrees well with experiment (18). In Fig. 5, the way the atoms shift in the transformation is marked by arrows in the 7-GPa geometry (see magnification).

The phase transition may be tracked in another way. Fig. 6 shows the calculated volume as a function of pressure (V-P curve) for CdSe nanosheets with adsorbed surfactants. There is an initial sharp decrease in volume between 0 GPa and 2.5 GPa. This volume reduction of 34% is likely due to relatively facile squeezing out of van der Waals space between ligand layers. Such behavior has been observed in molecular crystals under pressure (30). Another volume jump at 7 GPa is observed in the V-P curve, indicative of a phase transition. From the detailed atomic coordinates shown in Fig. 5, it may be seen that this is the wurtzite → rock salt transition in the CdSe nanolayer. In the transition zone, the corresponding volume reduction is 11%, as shown in Fig. 6. Note that there is a small enthalpy difference ($\Delta H = H_{7\,GPa} - H_{8\,GPa}$) of 2.38 eV per unit cell ($Cd_{14}Se_{14}$), at this transition, as shown in Fig. 6 *Inset*.

The phase transition is "delayed" by the dimensionality and/or coordination to surfactant molecules. To check the effect of surfactants on the phase transition, the seven-layer CdSe slab without methylamines was optimized at 5 GPa and higher pres-
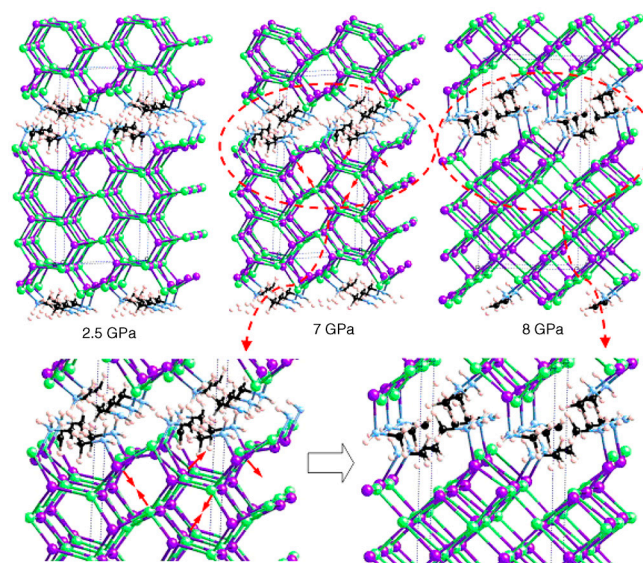

Fig. 5. Seven-layer CdSe slab with methylamines optimized at 2.5 GPa, 7 GPa, and 8 GPa. Two magnifications of the CdSe slab at 7 GPa and 8 GPa (red dotted ellipse zone) are shown, respectively. The atoms shifts are schematically shown by arrows in the optimized slab structure at 7 GPa. Cd atoms are in purple, Se atoms in green, C atoms in black, N atoms in blue, and H atoms in pink.
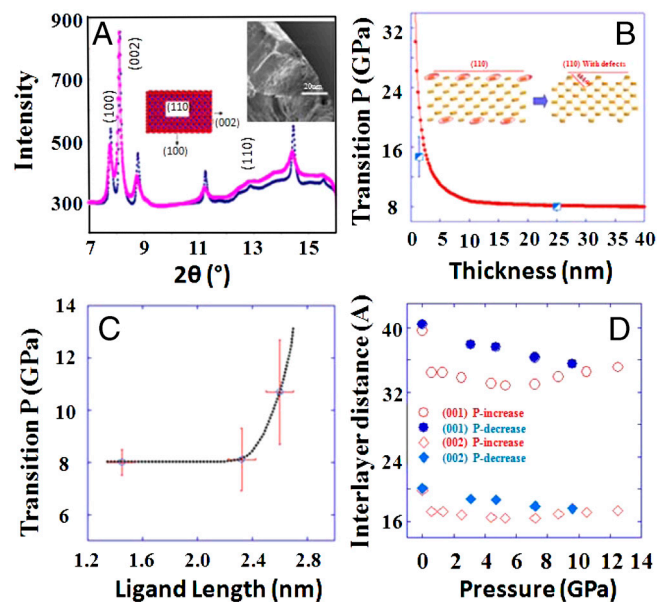
Fig. 6. Volume versus pressure curve of CdSe slab. (*Inset*) The relative enthalpy as a function of pressure.

Fig. 8. Schematic drawing of the relationship between the perfect rock-salt CdSe (110) surface and the CdSe part of "rock-salt phase" CdSe nanosheets.

sures; a rock-salt phase was obtained (see *SI Text* and Fig. S9). Thus, the coordination to surfactants is the important factor in delaying the phase transition.

3. Pressure-Tuned Rock-Salt CdSe Nanosheets. The simulated X-ray diffraction patterns of the seven-layer CdSe slab at 7 GPa and 8 GPa are shown in Fig. 7*A*, respectively. The λ used is 0.486 Å, the same λ as in the experimental study. A great difference in the X-ray diffraction pattern at 7 GPa and 8 GPa is observed, indicating that the structure has changed markedly. The simulated X-ray diffraction patterns agree reasonably well with the results obtained in our experiment (see Fig. 2). The nanosheets, even if they are seven layers thick, are quite different from the bulk, as the contrast between the diffraction patterns of bulk wurtzite and rock-salt CdSe (Fig. 7*B*) and the nanosheets (Fig. 7*A*) indicates.

In Fig. 8, we show schematically the relationship between an ideal rock-salt CdSe (110) surface (cut from bulk) and the rock-salt phase CdSe slab studied. In the structure given by our experimental and theoretical results, one can see a relationship between the saw-like rock-salt phase CdSe slab and potential defects in an ideal rock-salt CdSe (110) surface; the light red ellipses show the missing atoms. One can also perceive in the saw-like structure small facets of the rock-salt CdSe (001) surface.

4. Electronic Structure of CdSe Nanosheets Under High Pressure. Let us look at the electronic structure of the CdSe slabs. Fig. 9*A* shows the total density of states (TDOS) of CdSe slabs (with ligands) at 7 GPa and 8 GPa. The calculated gap of the CdSe slab at 7 GPa is around 1.7 eV. The wurtzite CdSe slab inherits its bulk semiconducting character; the analogous gap in bulk CdSe is calculated as 1.6 eV (shown in Fig. 9*B*). These gaps are too small—

experimentally the bulk gap is 1.7 eV and the nanosheet (at $P = 1$ atm) gap is 2.6 eV (26). DFT calculations typically underestimate band gaps in semiconductors (31). At 8 GPa, the rock-salt CdSe slab has a very small gap between its conduction and valence band. Again, this is similar to the rock-salt bulk phase (shown in Fig. 9*B*). The CdSe slabs still "remember" their corresponding bulk character.

5. Mechanical Stability and Strength of CdSe with Respect to the Embedded Soft Lligands. Comparison of the FWHM of the (002) peak of starting and recovered CdSe, along with observation of the SEM image of the recovered samples, indicates that wurtzite CdSe nanosheets do not undergo either a pressure- or transformation-induced fracture (Fig. 10*A*). However, fracture was observed at lower pressure in large-scale two-dimensional CdSe and ZnS nanocrystals without surface-ligand bonding (32–34). Similarities in structure and properties of several related semiconductors allow one to correlate CdS and CdTe, and to estimate the elastic strengths of CdSe (35, 36). We estimate that a 1.4-nm CdSe nanosheet has a yield strength of 4.4–6.8 GPa, which matches well the theoretical strength of 5.3 GPa. [Experiments show that 200- to 450-nm CdS nanocrystals and 15-nm CdTe tetrapods have an experimental yield strength of 2.2 and 2.6 GPa (35, 36), and their ideal yield strengths are estimated as 4.6 GPa and 6.0 GPa by the Griffith standard of $\sim E/10$ (*E*, Young's modulus). Extrapolating these results to CdSe, CdSe should have a yield strength close to 2.4 GPa (2.2–2.6 GPa). Fracture was observed at a transition pressure of 4 GPa in a 25-nm CdSe nanoribbon (33), but no fracture was observed at 10.7 GPa in 1.4-nm-thick nanosheets. Thus we are able to estimate the yield strength to be 4.4–6.8 GPa. Using $E = 53$ GPa for bulk CdSe (18), the ideal yield strength of CdSe was calculated to be 5.3 GPa.] Compared to bulk CdSe, the 1.4-nm thick CdSe nanosheets display a dramatical elevation of structural stability and remarkable enhancement of elastic strengths (e.g., yield strength and fracture toughness).

The enhancement of structural stability and elastic strength of lamellar CdSe nanosheets can be correlated with the presence of surface-bonded soft organic ligands. The low surface energy of the (110)-facet dominated morphology (37) of the nanosheet is also likely to be a stabilizing factor, but until we have nanosheets based on other crystal facets we will not know this for certain. The dependence of calculated transformation pres-

Fig. 7. Simulated X-ray diffractions using the source of synchrotron at the λ of 0.486 Å: (*A*) seven-layer CdSe slab; (*B*) bulk wurtzite and rock-salt CdSe.

Fig. 9. Computed TDOS: (*A*) seven-layer CdSe slab at 7 GPa and 8 GPa; (*B*) bulk wurtzite and rock-salt CdSe at ambient pressure.

Fig. 10. (*A*) Comparison of the FWHMs of the starting and recovered CdSe and SEM image of the recovered wurtzite from 12.7 GPa, indicative of no fracture through a cycle of pressurization/depressurization; (*B*) calculated thermodynamic transition pressure as a function of sheet thickness and resultant saw-like rock-salt layer; (*C*) observed transformation pressure in a 1.4-nm CdSe nanosheet as a function of intersheet ligand length; (*D*) pressure dependence of intersheet distance.

sure on sheet thickness (Fig. 10*B*) shows that reduction of nanosheet thickness leads to the rock-salt structure nucleating at ~14 GPa. [Calculations indicate that the (110) facet has the lowest surface energy (of 0.34 J/m^2) among all crystallographic facets that may contribute to the total internal energy (33), so we added this surface energy contribution to calculate the transformation pressure. In practical calculations, an average surface energy of 0.64 J/m^2 was used for the rock-salt phase.] This is slightly greater than the observed pressure of 10.7 GPa. However, surface ligands bond to the low energy (110) facets, thus making unlikely a possible role of the surface energy. And this ligand bonding is mainly responsible for the increased stability of the wurtzite structure. A plot of the transformation pressure as a function of ligand length in Fig. 10*C* allows us to define a critical length of ~2.3 nm as responsible for the dramatic alteration of the transformation pressure.

When the thickness of a CdSe nanosheet is less than 2.3 nm, the sheet displays a constant transformation pressure of ~8.1 GPa. Therefore, it is reasonable to use a short ligand (CH$_3$-NH$_2$) in computations on CdSe nanosheets, for studying the effect of the ligands on the phase transformation. The CH$_3$-NH$_2$ bonded CdSe nanosheets transform from a wurtzite to a rock-salt structure at 8.0 GPa; without ligand bonding, a lower transformation pressure of 5 GPa was found (Fig. S9). This difference suggests that in the absence of coordinating stabilizing ligands, the nanosheets will collapse to the bulk structures, leading to a transition pressure only slightly greater than the two pressures of 4.0 GPa and 2.5 GPa (observed in 25-nm-thick nanobelt and bulk CdSe), respectively (18, 33). Surface-bonded ligands thus appear to take on a simple and important role in preventing nanosheets from direct interactions.

The elastic properties of lamellar CdSe nanosheets, such as yield strength and fracture toughness, as well as their dependence on coordinating ligand length, may be both evaluated by variation of internanolayer distance as a function of pressure, using in situ pressure SAXRD (Fig. 10*D*). The distances between nanosheets initially display a normal pressure-dependent reduction, but an unusual expansion appears at 6.5 GPa. Once the internanosheet

spacing reaches 3.6 nm at 10.7 GPa, the interlayer distances remain constant. This unexpected phenomenon can be explained by the pressure-tuned changes of the chain structures and consequent lengths of octylamine and oleylamine. [An octylamine molecule has a chemical formula of C$_8$H$_{19}$N with a chain length of ~1.2 nm (1.0–1.2 nm), and we could assume that such a short chain is straight in the absence of external pressure. An oleylamine molecule, C$_{18}$H$_{37}$N, has a chain length of ~2.0 nm, but it is mostly buckled with variable angles from case to case, ranging from 1.5 to 1.8 nm (Fig. S1).]

The slightly buckled and tilted ligand chains attached to two nearby nanosheets we believe penetrate through the chain-chain gap. When the longer and buckled oleylamine chains arrive at the opposite CdSe nanosheet at 6.5 GPa, the buckled oleylamine chains may open up, and upon compression to 10.7 GPa, they may straighten (see cartoon in Fig. 11). We are going to study this process theoretically in the future. Unloading pressure results in complete recovery of the internanosheet distance (Fig. 10*D*), indicative of an elastic deformation during compression from 0 to 12.7 GPa. Obviously, additional interplay of surface ligands with brittle CdSe results in the enhanced elastic properties. The shear stress, as the key tuning factor for material fracture, is absorbed by the sandwiched soft materials. But when soft materials reduce the length scale, the absorption ability weakens and thus enhances the sheet–sheet interaction.

6. Perspectives and Unique Material Design. Our unique in situ nano-single-crystal-like X-ray diffraction technique, applied here to surface-bonded CdSe nanosheets, has great potential. The methodology is capable of directly monitoring and mapping pressure-driven atomic position changes, allowing for a reasonably straightforward reconstruction of the transformation pathway.

With the transformation-pathway-associated energy profile in hand, we are able to design previously undescribed groups of metastable high-energy structure materials that not only possess high density and hardness, but also manifest unique properties. Like the dense rock-salt CdSe phase, we could either dope other ions or tune particle size and morphology to build an energy barrier between wurtzite and rock salt. This barrier could effectively block the reverse structural change from rock salt to wurtzite, allowing the rock-salt geometry to be retained at ambient conditions (38, 39). For instance, cubic diamond persists at ambient conditions due to an energy barrier, but hexagonal diamond faces a small energy barrier and reverts back to graphite (39). Furthermore, the low surface energy facets tune the structural stability, and the surface-bonded soft ligands act as a shear stress absorber to enhance elastic strength. With the defined critical length scale and the recognized interplay between soft materials and brittle components, we may develop superb strong building blocks that extend elastic strength to its theoretical maximum.

Materials and Methods

Please see *SI Text* to this paper for details of the synthesis of the nanosheets, their structural characterization, the setup for the high pressure SAXRD and WAXRD measurements, and the computational modeling of the nanosheets under pressure.
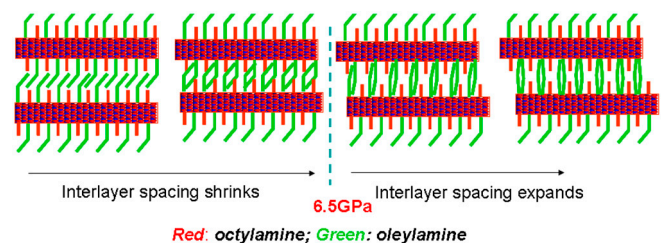

Fig. 11. Schematic drawing of the pressure-induced changes in mesostructured CdSe nanosheets.

1. McMillan PF (2002) New materials from high-pressure experiments. *Nat Mater* 1:19–25.
2. Aizenberg J, et al. (2005) Skeleton of *Euplectella* sp.: Structural hierarchy from the nanoscale to the macroscale. *Science* 309:275–278.
3. Peterlik H, Roschger P, Klaushofer K, Fratzl P (2006) From brittle to ductile fracture of bone. *Nat Mater* 5:52–55.
4. Bundy FP (1963) Direct conversion of graphite to diamond in static pressure apparatus. *J Chem Phys* 38:631–635.
5. Zhao YS, et al. (2004) Enhancement of fracture toughness in nanostructured diamond–SiC composites. *Appl Phys Lett* 84:1356–1358.
6. Riedel R (2000) *Handbook of Ceramic Hard Materials* (Wiley-VCH, Weinheim, Germany).
7. Desgreniers S, Beaulieu L, Lepage I (2000) Pressure-induced structural changes in ZnS. *Phys Rev B* 61:8726–8733.
8. Uchino M, et al. (1999) Phase transition and EOS of zinc sulfide (ZnS) under shock and static compressions up to 135 GPa. *J Phys Chem Solid* 60:827–837.
9. Yu SC, Spain IL, Skelton EF (1978) High pressure phase transitions in tetrahedrally coordinated semiconducting compounds. *Solid State Commun* 25:49–52.
10. Onodera A, Ohtani A (1980) Fixed points for pressure calibration above 100 kbars related to semiconductor-metal transitions. *J Appl Phys* 51:2581–2585.
11. Zhou Y, Cambell AJ, Heinz DH (1991) Equations of state and optical properties of the high pressure phase of zinc sulfide. *J Phys Chem Solids* 52:821–825.
12. Jaffe JE, Pandey R, Seel MJ (1993) Ab initio high-pressure structural and electronic properties of ZnS. *Phys Rev B* 47:6299–6303.
13. Nazzal A, Qteish A (1996) Ab initio pseudopotential study of the structural phase transformations of ZnS under high pressure. *Phys Rev B* 53:8262–8266.
14. Ves S, Schwarz U, Christensen NE, Syassen K (1990) Cubic ZnS under pressure: Optical-absorption edge, phase transition, and calculated equation of state. *Phys Rev B* 42:9113–9118.
15. Wang ZW, Guo QX (2009) Size-dependent structural stability and tuning mechanism: A case of zinc sulfide. *J Phys Chem C* 113:4286–4295.
16. Nieh TG, Wadsworth J (1991) Hall–Petch relation in nanocrystalline solids. *Scripta Metall Mater* 25:955–958.
17. Gao H, Ji B, Jager IJ, Arzt E, Fratzle P (2003) Materials become insensitive to flaws at nanoscale: Lessons from nature. *Proc Natl Acad Sci USA* 100:5597–5600.
18. Tolbert SH, Alivisatos AP (1995) The wurtzite to rock salt structural transformation in CdSe nanocrystals under high pressure. *J Chem Phys* 102:4642–4656.
19. Chen CC, et al. (1997) Size dependence of structural metastability in semiconductor nanocrystals. *Science* 276:398–401.
20. Jacobs K, Zaziski D, Scher EC, Herhold AB, Alivisatos AP (2001) Activation volumes for solid-solid transformations in nanocrystals. *Science* 293:1803–1806.
21. Wickham JN, Herhold AB, Alivisatos AP (2000) Shape change as an indicator of mechanism in the high-pressure structural transformations of CdSe nanocrystals. *Phys Rev Lett* 84:923–926.
22. Bealing C, Martonak R, Molteni C (2009) Pressure-induced structural phase transitions in CdSe: A metadynamics study. *J Chem Phys* 130:124712.
23. Grunwald M, Rabani C, Dellago C (2006) Mechanisms of the wurtzite to rocksalt transformation in CdSe nanocrystals. *Phys Rev Lett* 96:255701.
24. Zahn D, Grin Y, Leoni S (2005) Mechanism of the pressure-induced wurtzite to rocksalt transition of CdSe. *Phys Rev B* 72:064110.
25. Joo J, Son JS, Kwon SG, Yu JH, Hyeon T (2006) Low-temperature solution-phase synthesis of quantum well structured CdSe nanoribbons. *J Am Chem Soc* 128:5632–5633.
26. Son JS, et al. (2009) Large-scale soft colloidal template synthesis of 14 nm thick CdSe nanosheets. *Angew Chem Int Edit* 48:6861–6864.
27. Wenk HR, Can Houtte P (2004) Texture and anisotropy. *Rep Prog Phys* 67:1367–1428.
28. Sowa H (2005) The $CdSO_4$, rutile, cooperite and quartz dual nets: interpenetration and catenation. *Solid State Sci* 5:73–78.
29. Sowa H (2005) The high-pressure behavior of CdSe up to 3 GPa and the orientation relations between its wurtzite- and NaCl-type modifications. *Solid State Sci* 7:1384–1389.
30. Grochala W, Hoffmann R, Feng J, Ashcroft NW (2007) The chemical imagination at work in very tight places. *Angew Chem Int Edit* 46:3620–3642.
31. Hafner J (2008) Ab-initio simulations of materials using VASP: Density-functional theory and beyond. *J Comput Chem* 29:2044–2078.
32. Zaziski D, et al. (2004) Critical size for fracture during solid-solid phase transformations. *Nano Lett* 4:943–946.
33. Wang ZW, Finkelstein K, Ma C, Wang ZL (2007) Structure stability, fracture, and tuning mechanism of CdSe nanobelts. *Appl Phys Lett* 90:113115.
34. Wang ZW, et al. (2005) Morphology-tuned wurtzite-type ZnS nanobelts. *Nat Mater* 4:922–927.
35. Fang L, et al. (2007) Mechanical and electrical properties of CdTe tetrapods studied by atomic force microscopy. *J Chem Phys* 127:184704.
36. Shan ZW, et al. (2008) Ultrahigh stress and strain in hierarchically structured hollow nanoparticles. *Nat Mater* 7:947–952.
37. Manna L, Wang LW, Cingolani R, Alivisatos AP (2005) First-principles modeling of un-passivated and surfactant-passivated bulk facets of wurtzite CdSe: A model system for studying the anisotropic growth of CdSe nanocrystals. *J Phys Chem B* 109:6183–6192.
38. Jacobs K, Wickham J, Alivisatos AP (2002) Threshold size for ambient metastability of rocksalt CdSe nanocrystals. *J Phys Chem B* 106:3759–3762.
39. Wang ZW, et al. (2008) X-ray induced synthesis of 8H diamond. *Adv Mater* 20:3303–3307 and references therein.